Fast Start-Up Control of Both-Side Current without Overshoot Focusing on Rectification Timing for Dynamic Wireless Power Transfer Systems

Takumi Hamada, *Student Member, IEEE,* Toshiyuki Fujita, *Member, IEEE,* and Hiroshi Fujimoto, *Senior Member, IEEE*

***Abstract*—The paper proposes a method to improve the transient characteristics of current overshoot and oscillation at the start of power transmission for a dynamic wireless power transfer system. The system is important to reduce the settling time as short as possible without current overshoots for a stable power supply. However, conventional methods to suppress current overshoot have a slow response on the secondary side. This paper proposes the superposition of primary and secondary responses. The proposed method controls the secondary voltage by comparing the steady-state current with the current value on the secondary side. The method can effectively suppress the oscillations in the transient response by applying the secondary voltage at the appropriate timing. This paper also studied the robustness of constraints based on model analysis and experimental verification. In the experiments, the proposed method reduces the current overshoot and the settling time of the secondary current, and maximizes the receiving energy.**

***Index Terms*—Electric Vehicle, Wireless Power Transfer, Transient Control, Active Rectification, Inductive Power Transfer**

I. Introduction

Wireless power transfer (WPT) technology has been widely studied for many years [1]–[3]. In particular, WPT using magnetic resonant coupling has the features of high efficiency and high power transmission even with a large air gap and a lateral misalignment. From these advantages, WPT technology has attention for applications in various industrial fields [4], [5]. One of these is electric vehicles (EVs). It is expected that battery EVs will become more widespread to realize sustainable development goals.

However, electric vehicles have the problem of a shorter driving distance per charge compared to conventional vehicles such as internal combustion engines and hybrid-electric. It is due to the low energy density of the battery, and a larger battery capacity is required to solve the problem. On the other hand, increasing the battery size causes the heavy weight of the vehicle body and the long charging time. Therefore, dynamic wireless power transfer (DWPT) technology, which applies WPT technology to driving EVs, is researched sprightly. It can provide a solution to the problems of existing EVs. Furthermore, since the energy consumed is immediately recharged, the battery capacity can be reduced [6].

DWPT systems have several challenges compared to static WPT systems [7]. These include power fluctuations due to misalignment, which easily occurs, and optimum circuit configuration in large systems [8]–[12]. In addition, one of them is the limited time of power transmission. Therefore, the settling time during power transmission should be as short as possible. Also, it is essential to provide a stable power supply without an excessive current. DWPT systems tend to change coupling more than SWPT systems and it causes to fluctuate the power and currents. Furthermore, current pulsations during transients likely generate momentarily excessive currents compared to the steady-state value. Currents above the rated current not only increase the stress on the power-switching devices but also generate extremely high voltages in the coils and resonant capacitors. High voltages increase the rating of the equipment and lead to increased costs. In the worst case, the circuit components can be damaged. Thus, it is necessary to ensure sufficient power without excessive currents during transients [13].

Studies focusing on the transient characteristics of WPT are in modeling the dynamic behavior of the plant and control methods based on this model [14], [15]. The plant dynamics of a WPT system are broadly attributed to two types due to the resonant circuit and the response after the rectifier on the secondary side. In the resonant circuit, circuit compensation schemes and their modeling are considered, such as S-S, double-sided LCC [16], and LCC-S [17]. The characteristics after the rectifier are considered for smoothing capacitor and resistor load [18], [19], DC-DC converter [20], [21], and constant-voltage load circuit [22]. Compared to resonant circuits, the dynamics after the rectifier in smoothing capacitors and DC-DC converters tend to have relatively slow dynamics. Also, there are modeling by a resistor load, but this is not appropriate when discussing transient response accurately [23]. Assuming a charge to EV's battery, a constant voltage load can best simulate the dynamic behavior. This study focuses on the dynamics of the resonant circuit section, especially the transient characteristics at the start of transmission.

Many previous studies focusing on the start of power transmission deal with primary side control [24]–[26]. One of the simple methods to suppress the current overshoot use phase-shift control in a full-bridge inverter [27], [28]. Also, methods using frequency modulation have been proposed [29]. However, these methods are less theoretically based on transient models. [19] and [30] proposed approaches using model predictive control. On the other hand, there are disadvantages in that bilateral communication is required. In [30], a fast response of the secondary current is realized, but instantaneous current overshoots are not suppressed sufficiently. The studies in [22] and [31] focused on the moment when the diode

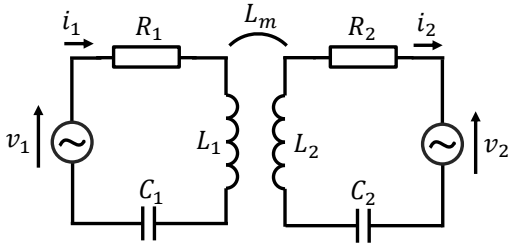

Fig. 1: S-S compensated equivalent circuit model for WPT.

rectifier conducts and proposed control methods that do not occur overshoots. These methods suppress current overshoots by controlling the fundamental amplitude of the primary voltage. However, the time when the secondary current settles becomes longer due to the smaller voltage in the transient section. In many previous studies, the settling time of the secondary current is in the order of several ms. As above, the settling time is also an important factor in DWPT systems.

Therefore, this paper proposes the transient control method at the start of power transmission that satisfies both requests. The proposed method is a simple way to compare the reference value. It focuses on the superposition of transient responses and cancels them out using an active rectifier on the secondary side. It has the advantage of the settling time being about the order of μs.

The basic idea has already been proposed in [32]. [32] verified the overshoot and settling time effectiveness of the start-up current control using the secondary side. However, it dealt with only a static condition. It was also evaluated on the confined condition the constraints are met. The difference from [32] is that this study analyses the robustness against the constraints of the proposed method based on the model analysis and experiments. Also, the proposed method is applied to the moving coil bench, or DWPT bench, and evaluates the effectiveness of the receiving energy.

This paper is organized as follows: First, section Ⅱ explains the derivative of a simple envelope model using the features of the WPT circuit to deal with the start of power transmission. Second, section Ⅲ shows the proposed method to suppress current overshoots using the secondary side. In addition, it also considers the robustness of the proposed method. In section I V, the experimental setup and the results of the experiments using the proposed method are described. In the experiments, the robustness is evaluated based on static WPT experiments. Furthermore, the proposed method was applied to a moving coil bench. Finally, in Section V, conclusions are presented.

II. Derivation of the envelope model.

Fig. 1 shows an S-S compensated equivalent circuit model for WPT. The R_i, L_i, and C_i are the internal resistance, the self-inductance, and the resonant capacitor of each coil, respectively. The subscript $i = 1, 2$ means the primary and the secondary sides. The resonant capacitor is designed to satisfy the following resonance conditions.

$$\omega = \frac{1}{\sqrt{L_1 C_1}} = \frac{1}{\sqrt{L_2 C_2}}. \tag{1}$$

L_m is the mutual inductance and has the following relation to the coupling coefficient k.

$$k = \frac{L_m}{\sqrt{L_1 L_2}}. \tag{2}$$

The primary voltage v_1 works at the same operating frequency ω_o as the resonant frequency ω. Also, the output voltages of the inverter and the rectifier are originally square waves, however, the WPT circuit has bandpass characteristics and the currents become sine waves of the resonant frequency. Therefore, this study focuses on the fundamental components of each AC waveform. Based on approximation, the primary voltage is expressed as follows [31]:

$$v_1 = V_1(t) \sin \omega t, \tag{3}$$

where $V_1(t)$ is the fundamental amplitude of v_1.

Assuming that the effect of forced oscillations is dominant due to the Q of the resonant circuit being sufficiently large, the phase of the primary current i_1 is the same as the phase of v_1 and is expressed as

$$i_1 = I_1(t) \sin \omega t, \tag{4}$$

where $I_1(t)$ is the fundamental amplitude of i_1. Furthermore, the secondary current i_2 lead to 90 degrees relative to v_1 and is expressed as

$$i_2 = I_2(t) \cos \omega t, \tag{5}$$

where $I_2(t)$ is the fundamental amplitude of i_2. In the same way, the secondary voltage v_2 is

$$v_2 = V_2(t) \cos \omega t, \tag{6}$$

where $V_2(t)$ is the fundamental amplitude of v_2.

Using Eq. (1)-Eq. (6) under the perfect resonance assumption of $\omega_o = \omega$, each current and voltage substitute the circuit equation of Fig. 1, and each term is calculated as follows:

$$L_1 \frac{di_1}{dt} = L_1 \frac{dI_1}{dt} \sin \omega t + \omega L_1 I_1 \cos \omega t, \tag{7}$$

$$\begin{aligned} \frac{1}{C_1} \int i_1 \, dt &= \frac{-I_1}{\omega C_1} \cos \omega t + \frac{1}{\omega^2 C_1} \frac{dI_1}{dt} \sin \omega t - \frac{1}{\omega^2 C_1} \int \frac{d^2 I_1}{dt^2} \sin \omega t \, dt \\ &\approx \frac{-I_1}{\omega C_1} \cos \omega t + \frac{1}{\omega^2 C_1} \frac{dI_1}{dt} \sin \omega t, \end{aligned} \tag{8}$$

$$\begin{aligned} \frac{d}{dt}(L_m i_2) &= \frac{dL_m}{dt} I_2 \cos \omega t + L_m \frac{dI_2}{dt} \cos \omega t - \omega L_m I_2 \sin \omega t \\ &\approx L_m \frac{dI_2}{dt} \cos \omega t - \omega L_m I_2 \sin \omega t \quad \left(\because \frac{dL_m}{dt} \ll 1 \right), \end{aligned} \tag{9}$$

where the amplitude is the function of time and Eq. (8) neglects the third and from higher orders because $1/\omega$ appears every time to calculate a partial integral. In Eq. (9), $\frac{dL_m}{dt}$ is expressed as $\frac{dL_m}{dx}\frac{dx}{dt}$ and this value is sufficiently negligible [33]. Therefore, the circuit equations on the primary side are expressed as

$$\begin{aligned} \left(2L_1 \frac{dI_1(t)}{dt} + R_1 I_1(t) - V_1(t) + \omega L_m I_2(t) \right) \sin \omega t \\ + L_m \frac{dI_2(t)}{dt} \cos \omega t = 0. \end{aligned} \tag{10}$$

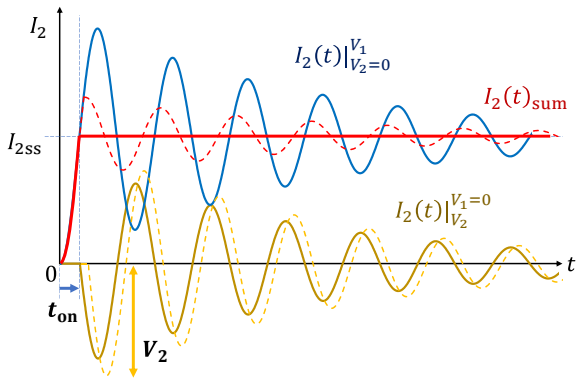

Fig. 2: Diagram of timing adjustment of active rectification: shows envelop model step responses $I_2(t)|_{V_2=0}^{V_1}$ and $I_2(t)|_{V_2}^{V_1=0}$. The sum of each response $I_2(t)_{\mathrm{sum}}$ is an actual circuit response. The solid line is the ideal response wave.

Assuming the coupling coefficient is small and $2L_1 \gg L_m$ holds in the DWPT system, the second term of Eq. (10) is neglected. Due to Eq. (10) holds at any t, the equation of the amplitudes can be obtained. In the same way, the secondary-side equation can be calculated under $2L_2 \gg L_m$. From the above, the simplified envelope model which does not include fundamental frequency can be derived as follows:

$$\begin{cases} 2L_1 \dfrac{dI_1(t)}{dt} + R_1 I_1(t) = V_1(t) - \omega L_m I_2(t), \\ 2L_2 \dfrac{dI_2(t)}{dt} + R_2 I_2(t) = \omega L_m I_1(t) - V_2(t). \end{cases} \tag{11}$$

III. Strategy for start-up current control

Section III-A shows the main idea of the control strategy, III-B analyzes the robustness of the proposed method, and III-C is the implementation method.

A. Overshoot Suppression Focusing on the Response Superposition

As the input variables are the voltage amplitudes $(V_1, V_2)^{\mathrm{T}}$ and the output variables are the current amplitudes $(I_1, I_2)^{\mathrm{T}}$, the Laplace transform of Eq. (11) is calculated as

$$\begin{pmatrix} I_1 \\ I_2 \end{pmatrix} = \frac{\omega_{\mathrm{n}}^2}{s^2 + 2\zeta\omega_{\mathrm{n}} s + \omega_{\mathrm{n}}^2 + \alpha_1\alpha_2} \cdot \begin{pmatrix} \frac{1}{2L_1}\frac{1}{\omega_{\mathrm{n}}^2}(s+\alpha_2) & \frac{1}{\omega L_m} \\ \frac{1}{\omega L_m} & -\frac{1}{2L_2}\frac{1}{\omega_{\mathrm{n}}^2}(s+\alpha_1) \end{pmatrix} \begin{pmatrix} V_1 \\ V_2 \end{pmatrix}, \tag{12}$$

where

$$\alpha_1 = \frac{R_1}{2L_1}; \quad \alpha_2 = \frac{R_2}{2L_2}; \quad \omega_{\mathrm{n}} = \frac{\omega k}{2}; \quad \zeta = \frac{1}{2}\left(\frac{1}{Q_1} + \frac{1}{Q_2}\right)\frac{1}{k}; \quad Q_1 = \frac{\omega L_1}{R_1}; \quad Q_2 = \frac{\omega L_2}{R_2}.$$

Generally, $\omega_{\mathrm{n}}^2 + \alpha_1\alpha_2 \approx \omega_{\mathrm{n}}^2$ holds owing to the WPT system meeting $\omega^2 L_m^2 \gg R_1 R_2$. Thus, Eq. (12) can be described as a second-order system in the standard form. It has poles p and the resonant frequency ω_{d} expressed as

$$p = -\zeta\omega_{\mathrm{n}} \pm j\omega_{\mathrm{n}}\sqrt{1-\zeta^2} = -\zeta\omega_{\mathrm{n}} \pm j\omega_{\mathrm{d}}. \tag{13}$$

where $\omega_{\mathrm{d}} \approx \omega_{\mathrm{n}}$ is met since ζ is the inverse of kQ.

The proposed method focuses on canceling the current overshoot and oscillation by superimposing responses of I_2 calculated from V_1 and V_2 at the appropriate time. Step responses $I_2(t)|_{V_2=0}^{V_1}$ which is the function from V_1 to I_2 and $I_2(t)|_{V_2}^{V_1=0}$ which from V_2 to I_2 are respectively calculated as follows:

$$\begin{aligned} I_2(t)|_{V_2=0}^{V_1} &= \frac{V_1}{\omega L_m}\left(1 - e^{-\zeta\omega_{\mathrm{n}}t}\cos\omega_{\mathrm{d}}t - \frac{\zeta}{\sqrt{1-\zeta^2}}e^{-\zeta\omega_{\mathrm{n}}t}\sin\omega_{\mathrm{d}}t\right) \\ &\approx \frac{V_1}{\omega L_m}\left(1 - e^{-\zeta\omega_{\mathrm{n}}t}\cos\omega_{\mathrm{n}}t\right), \qquad (\because \zeta \ll 1) \end{aligned} \tag{14}$$

$$\begin{aligned} & I_2(t)|_{V_2}^{V_1=0} \\ &= -\frac{R_1 V_2}{\omega^2 L_m^2}\left(1 - e^{-\zeta\omega_{\mathrm{n}}t}\cos\omega_{\mathrm{d}}t + \left(\frac{\omega_{\mathrm{n}}}{\alpha_1} - \zeta\right)\frac{1}{\sqrt{1-\zeta^2}}e^{-\zeta\omega_{\mathrm{n}}t}\sin\omega_{\mathrm{d}}t\right) \\ &\approx -\frac{V_2}{\omega L_m}\sqrt{\frac{L_1}{L_2}}e^{-\zeta\omega_{\mathrm{n}}t}\sin\omega_{\mathrm{n}}t. \qquad \left(\because \frac{\omega_{\mathrm{n}}}{\alpha_1} = kQ_1 \gg 1\right) \end{aligned} \tag{15}$$

The actual response of I_2 is a superposition of Eq. (14) and Eq. (15).

Fig. 2 shows a diagram of each response. Since $I_2(t)|_{V_2}^{V_1=0}$ oscillates in the negative direction, it is possible to weaken the transient response by inputting the oscillations of $I_2(t)|_{V_2}^{V_1=0}$. Then, the conditions for t_{on} and V_2 to obtain an ideal waveform like the solid line is considered.

From Eq. (14) and Eq. (15), each envelope response is inverse phase at the following t_{on}.

$$t_{\mathrm{on}} = \frac{\pi}{2\omega_{\mathrm{n}}} = \frac{\pi}{\omega k}. \tag{16}$$

Also, the secondary current at t_{on} is expressed as

$$I_{2\mathrm{th}} = I_2(t_{\mathrm{on}}) = \frac{V_1}{\omega L_m}. \tag{17}$$

This is the same as the steady-state value $I_{2\mathrm{ss}} \approx \frac{V_1}{\omega L_m}$.

Furthermore, considering conditions in which the amplitude of responses is exactly the same, it is expressed as

$$I_2(t + t_{\mathrm{on}})|_{V_2=0}^{V_1} + I_2(t)|_{V_2}^{V_1=0} = I_{2\mathrm{ss}}. \tag{18}$$

From Eq. (14)-Eq. (18), the following constraint can be obtained as

$$V_2 = e^{-\zeta\frac{\pi}{2}}\sqrt{\frac{L_2}{L_1}}V_1 \tag{19}$$

$$\approx \sqrt{\frac{L_2}{L_1}}V_1. \tag{20}$$

Thus when the condition of Eq. (20) is satisfied, the current overshoots during transient oscillations can be completely suppressed by applying for the secondary voltage V_2 after t_{on} Eq. (16) from the power transmission start. As described in section III-C, the implementation of the experiment adopts to determine the input timing by reference to the secondary

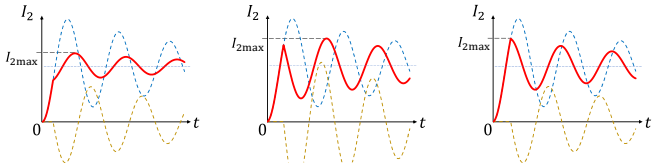

(a) Case 1 **(b)** Case 2 **(c)** Case 3

Fig. 3: Envelop waveform patterns of the secondary current when the proposed method is used.

current i_2. The above analysis assumes that L_m is a constant. However, even in DWPT systems with varying L_m, the change $\Delta L_m = L_m(t+t_{\rm on}) - L_m(t)$ is negligible because the time variation of L_m is small.

The proposed method is restricted by Eq. (20). However, an optimal voltage $V_{2\eta\rm opt}$ which realizes maximum efficiency is expressed as [20]

$$V_{2\eta\rm opt} = \sqrt{\frac{R_2}{R_1}} \frac{\omega L_m}{\sqrt{R_1R_2 + \omega^2 L_m^2} + \sqrt{R_1R_2}} V_1 \approx \sqrt{\frac{R_2}{R_1}} V_1. \quad (21)$$

Therefore, if assuming R has proportional relation to L approximately, note that the constraint is realistic.

B. Constraint Robustness of the Proposed Method

The constraints mentioned in section III-A are not always met due to variations in the coupling, the voltage, and sensor noises. Hence, this section calculates the maximum current $I_{2\max}$ at the rectification timing and secondary voltage which does not satisfy the conditions Eq. (16) and Eq. (20) to evaluate constraints robustness. As V_2 and $t_{\rm on}$ are variables, using Eq. (14) and Eq. (15), I_2 is expressed as follows:

$$\begin{aligned} I_2(V_2, t_{\rm on}, t) &= I_2(t + t_{\rm on})|_{V_{2=0}}^{V_1} + I_2(V_2, t)|_{V_2}^{V_1=0} \\ &= \frac{V_1}{\omega L_m} - \frac{e^{-\zeta\omega_{\rm n} t}}{\omega L_m} \left(A\cos\left(\omega_{\rm n} t + \omega_{\rm n} t_{\rm on}\right) + B\sin\omega_{\rm n} t\right), \end{aligned} \quad (22)$$

where

$$A = e^{-\zeta\omega_{\rm n} t_{\rm on}} V_1; \quad B = \sqrt{\frac{L_1}{L_2}} V_2; \quad \gamma = \frac{B}{A}.$$

A and B mean the amplitude of the response from V_1 and V_2. Then, γ means their ratio.

Fig. 3 shows the envelop waveform patterns of the secondary current. $I_{2\max}$ is classified by considering three different cases.

(a) Case 1: I_2 maximizes at the first peak.
(b) Case 2: I_2 maximizes at the second peak.
(c) Case 3: I_2 maximizes at the switching moment.

To classify patterns, the partial derivative to t of Eq. (22) is caluculated as follows:

$$\begin{aligned} \frac{\partial I_2(V_2, t_{\rm on}, t)}{\partial t} &= \left((A\sin\omega_{\rm n} t_{\rm on} - B - \zeta A\cos\omega_{\rm n} t_{\rm on})\cos\omega_{\rm n} t\right. \\ &\quad \left. - (\zeta(B - A\sin\omega_{\rm n} t_{\rm on}) + A\cos\omega_{\rm n} t_{\rm on})\sin\omega_{\rm n} t\right) \frac{\omega_{\rm n} e^{-\zeta\omega_{\rm n} t}}{\omega L_m} \\ &\approx \left((A\sin\omega_{\rm n} t_{\rm on} - B)\cos\omega_{\rm n} t - A\cos\omega_{\rm n} t_{\rm on}\sin\omega_{\rm n} t\right) \frac{\omega_{\rm n} e^{-\zeta\omega_{\rm n} t}}{\omega L_m}. \\ &\qquad (\because \zeta \ll 1) \end{aligned} \quad (23)$$

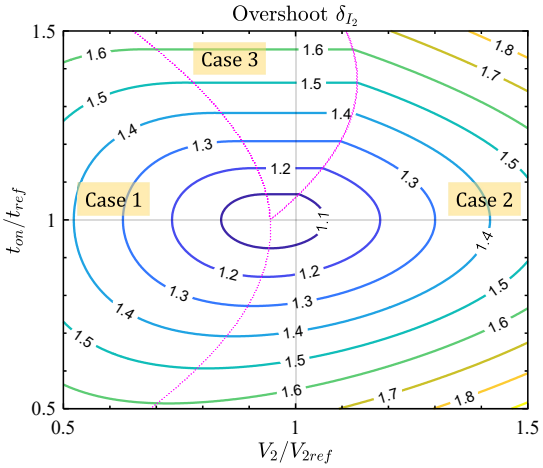

Fig. 4: Function $\delta_{I_2}(V_2, t_{\rm on})$ of V_2 and $t_{\rm on}$. Each axis is normalized by the constraints.

The candidate of the maximum secondary current $I_{2\max}$ and the time $t = t_{\rm m}$ at $I_{2\max}$ satisfy

$$\frac{\partial I_2(V_2, t_{\rm on}, t = t_{\rm m})}{\partial t} = 0. \quad (24)$$

The sign of the derivative at the switching time, i.e. $t = 0$, determines case 1 and case 2 as follows:

$$\frac{\partial I_2(V_2, t_{\rm on}, t = 0)}{\partial t} > 0, \quad \text{if case 1} \quad (25)$$

$$\frac{\partial I_2(V_2, t_{\rm on}, t = 0)}{\partial t} \le 0. \quad \text{if case 2} \quad (26)$$

Case 3 is classified when Eq. (26) is met and satisfies

$$I_2(V_2, t_{\rm on}, t = 0) > I_2(V_2, t_{\rm on}, t = t_{\rm m}). \quad (27)$$

From Eq. (24)-Eq. (27), the time $t_{\rm m}$ when the current gets the maximum value is classified as

$$\omega_{\rm n} t_{\rm m}(V_2, t_{\rm on}) = \begin{cases} \phi_{\rm m1} & \text{if } D_1 < 0, \quad \text{case 1} \\ \phi_{\rm m2} + \pi & \text{if } D_1 > 0, D_3 < 0, \quad \text{case 2} \\ 0 & \text{if } D_1 > 0, D_3 > 0, \quad \text{case 3} \end{cases} \quad (28)$$

where

$$\phi_{\rm m1}(V_2, t_{\rm on}) = \arccos\frac{-D_2}{\sqrt{D_1^2 + D_2^2}}, \quad (0 \le \phi_{\rm m1} \le \pi)$$

$$\phi_{\rm m2}(V_2, t_{\rm on}) = \arccos\frac{D_2}{\sqrt{D_1^2 + D_2^2}}, \quad (0 \le \phi_{\rm m2} \le \pi)$$

$$D_1 = \gamma - \sin\omega_{\rm n} t_{\rm on},$$

$$D_2 = \cos\omega_{\rm n} t_{\rm on},$$

$$D_3 = -D_1^2 + (e^{2\zeta(\phi_{\rm m2}+\pi)} - 1)D_2^2.$$

From Eq. (28), the maximum current is calculated as

$$I_{2\max}(V_2, t_{\rm on}) = \frac{V_1}{\omega L_m}\left(1 + \delta_{I_2}(V_2, t_{\rm on}, t_{\rm m})\right), \quad (29)$$

$$\delta_{I_2}(V_2, t_{\rm on}) = \begin{cases} e^{-\zeta\phi_{\rm m1}} e^{-\zeta\omega_{\rm n} t_{\rm on}} \sqrt{D_1^2 + D_2^2}, & \text{if case 1} \\ e^{-\zeta(\phi_{\rm m2}+\pi)} e^{-\zeta\omega_{\rm n} t_{\rm on}} \sqrt{D_1^2 + D_2^2}, & \text{if case 2} \\ e^{-\zeta\omega_{\rm n} t_{\rm on}}(-D_2), & \text{if case 3} \end{cases} \quad (30)$$

TABLE I: Parameters in the experiment

Symbol	Definition	Value
f_o	Operating frequency	85 kHz
L_1	Transmitter inductance	124.49 µH
R_1	Transmitter resistance	144.42 mΩ
L_2	Receiver inductance	53.87 µH
R_2	Receiver resistance	120.09 mΩ
L_m	Mutual inductance	7.367 µH
E_1	Transmitting-side DC-link voltage	50 V
E_2	Receiving-side DC-link voltage	16-36 V

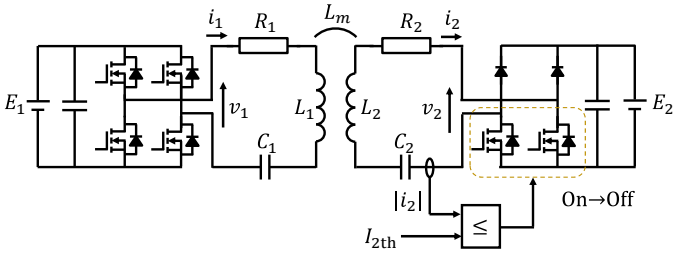

Fig. 5: WPT circuit configuration in experiment with proposed method.

where δ_{I_2} is the maximum overshoot rate of i_2.

Fig. 4 shows the relation of δ_{I_2} against V_2 and t_{on} from Eq. (30). Here, each axis is normalized by the constraints Eq. (16) and Eq. (20), and the parameters are Table I. The minimum $\delta_{I_2}(V_2, t_{\text{on}})$ is slightly shifted to the left due to approximation of Eq. (20). Using $\omega_{\text{n}} t_{\text{on}} - \pi/2 \ll 1$, the dominant value of Eq. (30) in cases 1 and 2 $\sqrt{D_1^2 + D_2^2}$ is caluculated as

$$\sqrt{D_1^2 + D_2^2} \approx \sqrt{(\gamma - 1)^2 + \gamma \left(\omega_{\text{n}} t_{\text{on}} - \frac{\pi}{2}\right)^2}. \tag{31}$$

It confirms that the closer the amplitude ratio γ between the primary and secondary sides is to 1 and the closer each amplitude envelope phase $\omega_{\text{n}} t_{\text{on}}$ is to the opposite, the more the overshoot is suppressed. Also, $\delta_{I_2}(V_2, t_{\text{on}})$ increases in approximate proportion to the amount of variation from the constraint when one of the constraints is met: e.g. $\sqrt{D_1^2 + D_2^2} \approx |\gamma - 1|$ holds when $\omega_{\text{n}} t_{\text{on}} = \pi/2$.

C. Implementation of the Voltage Step Input

Fig. 5 shows the circuit configuration in experiments. The input from V_2 on the secondary side is implemented using a semi-bridgeless active rectifier. The inverter on the primary side outputs an AC voltage and the secondary side connects a constant voltage load through the converter. The converter on the secondary side switches the lower arms to change short and open modes for controlling the voltage input time. By switching from short mode to open mode, the voltage amplitude $\frac{4}{\pi} E_2$ is added at the moment of conduction, thereby realizing a step input of voltage. Beside, it is not necessary to use the configuration of the Fig. 5, if it is possible to realize step voltage applications such as a full-bridge rectifier.

Based on the analysis of III-A, The switching time t_{on} is after the start of transmission. However, without communication between the primary and the secondary sides, the secondary side cannot get the exact transmission start time. Therefore, the switching time is determined by using the receiving current i_2 instead of t_{on}. The controller compares the measured absolute value of i_2 with the threshold value $I_{2\text{th}}$ given beforehand and outputs a switching signal.

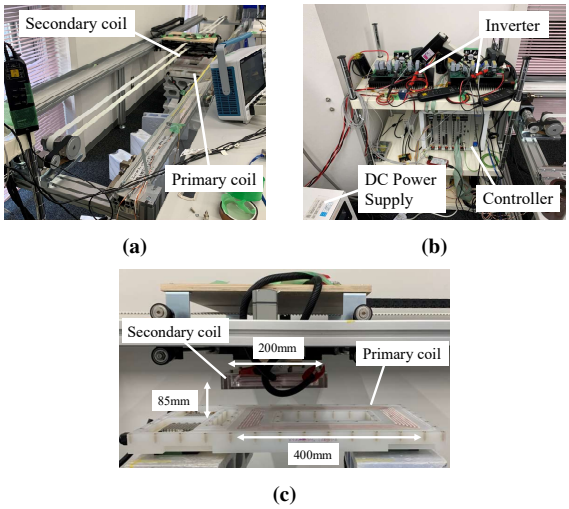

Fig. 6: Experimental setup (a) DWPT bench (b) Circuit equipment (c) Coils.

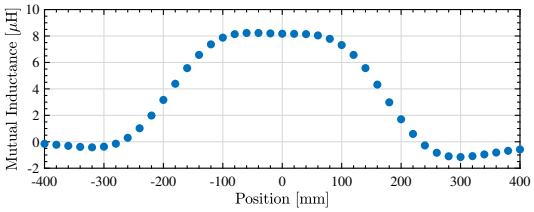

Fig. 7: Relation between position and coupling coefficient.

IV. Experimental Verification

Fig. 6 shows the experimental setup to demonstrate static (section IV-A) and dynamic (section IV-B) power transmission. Fig. 6(a) shows the moving coil bench. The secondary coil is able to move using a motor and a belt. The motor has an encoder to get an accurate position of the secondary coil. Fig. 6(b) shows the configuration of the power supply and its controller. The power supply works as a constant voltage load to emulate a battery. The inverter on the primary side and the converter on the secondary side are the same full-bridge inverter using SiC MOSFETs. The drive frequency of the inverter on the primary side is 85 kHz. The secondary side works as a semi-bridgeless active rectifier in this experiment. The controller is PE-Expert4 from Myway Plus Corporation, which uses an FPGA to generate optical signals and execute fast AD conversion at 4.2 MHz. The current sensor for AD conversion is CT6862-05 from HIOKI E.E. Corporation. Note that the same controller drives inverters in this experiment, but there is no information exchange between the primary and secondary sides. Fig. 6(c) shows a positional relation of coils.

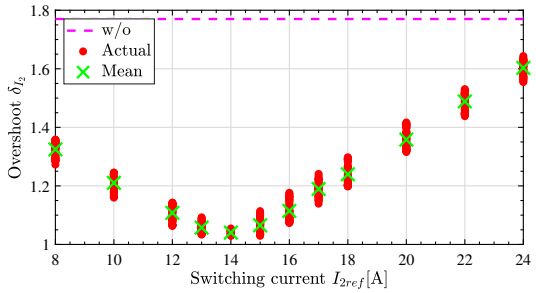

(a) Relation between $I_{2\mathrm{ref}}$ and $\delta_{I_2}(V_2, t_{\mathrm{on}})$.

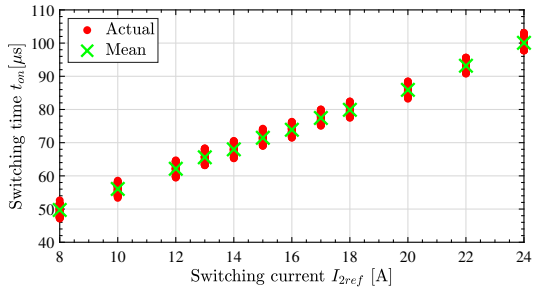

(b) Relation between $I_{2\mathrm{ref}}$ and t_{on}.

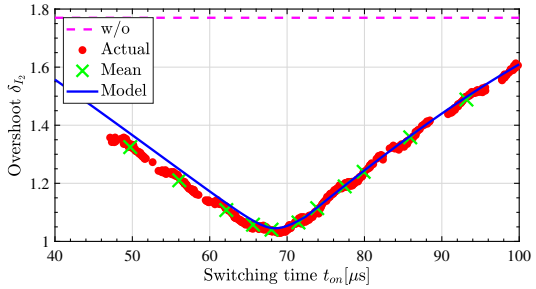

(c) Relation between t_{on} and $\delta_{I_2}(V_2, t_{\mathrm{on}})$.

Fig. 8: Experimental results of $\delta_{I_2}(V_2, t_{\mathrm{on}})$ when $I_{2\mathrm{ref}}$ changes and $E_{2\mathrm{ref}}$ is fixed.

The parameters in the experiment are shown in Table I. Here, L_m is the value of the static experiment. Fig. 7 shows the relation between position and L_m in the dynamic experiment.

A. Robustness Evaluation

This section evaluated the robustness of the constraints variation, i.e. the switching current and the secondary voltage. The current overshoot on the secondary side $\delta_{I_2}(V_2, t_{\mathrm{on}})$ was measured by varying one of the constraints and fixing the other. Also, analysis values at each axis derived in section III-B are compared with experimental values. The experiments were carried out 50 times since the measured values differ under the same experimental conditions. Then, the average values were calculated from the experimental results.

1) Robustness of I_{2ref}: The experiment was done with the fixed voltage satisfying Eq. (20), and the value $I_{2\mathrm{ref}}$ varied. Here, the voltage received takes into account the drop voltage during diode conduction. $I_{2\mathrm{ref}}$ is set from 8 to 24 A, which means by a factor of ±0.5 with the current constraint in Eq. (17).

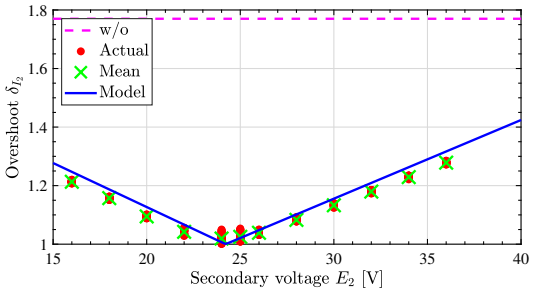

Fig. 9: Experimental results of $\delta_{I_2}(V_2, t_{\mathrm{on}})$ when E_2 changes and $I_{2\mathrm{ref}} = 14\,\mathrm{A}$ is fixed.

Fig. 8(a) shows the relation between $I_{2\mathrm{ref}}$ and $\delta_{I_2}(V_2, t_{\mathrm{on}})$ when $E_{2\mathrm{ref}}$ is fixed at 26 V from Eq. (20). The current $I_{2\mathrm{th}}$ is 16.16 A calculated by Eq. (17) . $\delta_{I_2}(V_2, t_{\mathrm{on}})$ is minimize at $I_{2\mathrm{ref}} = 14\,\mathrm{A}$ and it is a smaller current value than $I_{2\mathrm{th}}$. It means that the actual value of the steady-state current is smaller than expected by Eq. (17) due to the high resistance of the DWPT bench.

Fig. 8(b) shows the relation between $I_{2\mathrm{ref}}$ and the experimental t_{on}. t_{on} has a variation about 5 μs, which is about half the period of the operating frequency. In the experiments, the FPGA controller measures the instantaneous current value and compares its absolute value with the reference value to judge the switch MOSFETs as shown in Fig. 5. Therefore, this time variation is unavoidable in the implementation since a delay of up to $1/2f_o$ can occur depending on the rise of the current.

Fig. 8(c) shows the relation between t_{on} and $\delta_{I_2}(V_2, t_{\mathrm{on}})$ using Fig. 8(b). The model plots Eq. (30) at $V_2 = \sqrt{L_2/L_1}V_1$. It confirmed that the experimental and analytical values are in approximate agreement. The experimental values are slightly larger than the analytical values. It is considered due to a slight non-resonance. From these results, the proposed method can suppress the overshoot even if the no constraint conditions when compared to without control. Furthermore, $\delta_{I_2}(V_2, t_{\mathrm{on}})$ at $t_{\mathrm{on}} = 68\,\mu$s is less than 5 %. A sufficiently short settling time of the order of μs can be achieved without the overshoot under these conditions.

2) Robustness of V_2: The overshoot $\delta_{I_2}(V_2, t_{\mathrm{on}})$ was evaluated with the value E_2 varied from 16 to 36 V and the fixed $I_{2\mathrm{ref}}$, which was the minimum $\delta_{I_2}(V_2, t_{\mathrm{on}})$ in section IV-A1.

Fig. 9 shows the relation between E_2 and $\delta_{I_2}(V_2, t_{\mathrm{on}})$ when $I_{2\mathrm{ref}}$ is fixed at 14 A. At $I_{2\mathrm{ref}} = 14\,\mathrm{A}$, the average of the switching time t_{on} is 68 μs caluculated by Fig. 8(b). $E_{2\mathrm{ref}}$ is 26 V caluculated by Eq. (20). The model plots Eq. (30) at $\omega_{\mathrm{n}} t_{\mathrm{on}} = \pi/2$. The shift from $E_{2\mathrm{ref}}$ in the experimental and analytical values is due to the neglect of the coupling coefficient term in equation Eq. (20). The experimental $\delta_{I_2}(V_2, t_{\mathrm{on}})$ are smaller than the analytical values due to the same reason as in section IV-A1. Also, the results confirmed that the increase in $\delta_{I_2}(V_2, t_{\mathrm{on}})$ due to voltage changes is smaller than the one due to current changes. From the above, the proposed method can greatly suppress the overshoot than the case without control, even if the constraint of V_2 does not meet similarly section IV-A1. Also, at $E_2 = 24\,\mathrm{V}$, the average value of $\delta_{I_2}(V_2, t_{\mathrm{on}})$ is reduced to 2 %.

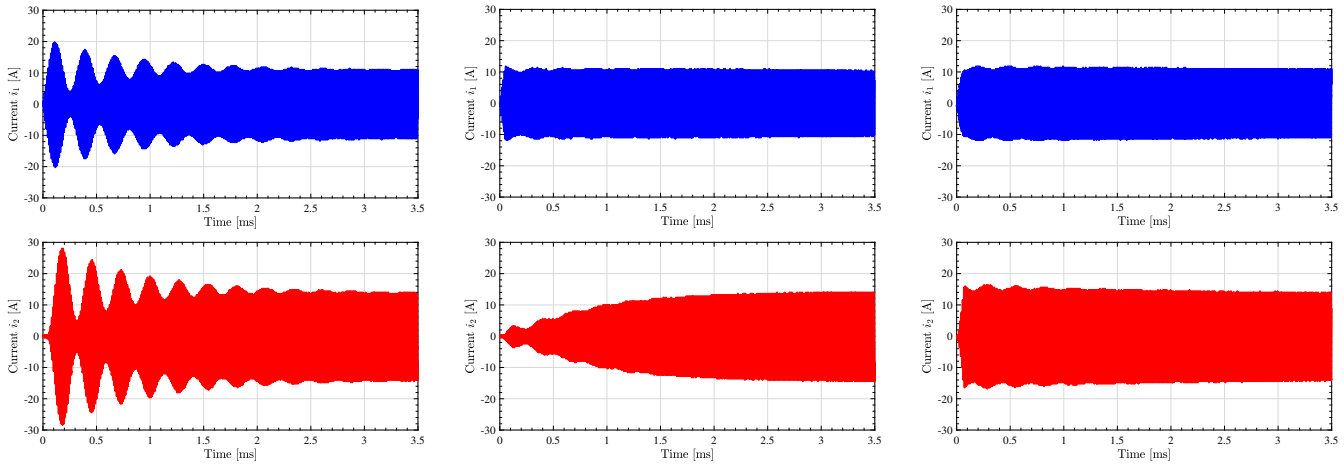

(a) Without control **(b)** Phase shift control [31] **(c)** Proposed method

Fig. 10: Experimental results of transient part using DWPT bench at 10 km/h. (blue: primary current i_1, red: secondary current i_2).

TABLE II: Experimental results using DWPT bench at 10 km/h.

Method	Max Current i_2 [A]	Receiving energy up to 3 ms [J]	Energy efficiency up to 3 ms [%]
Without control	28.0	0.885	93.4
Phase shift control [31]	14.2	0.614	91.9
Proposed method	16.0	0.877	93.6

B. Receiving Energy Evaluation using DWPT Bench.

To evaluate the effectiveness of the receiving power per transmission, an experiment was carried out using the DWPT bench shown in Fig. 6(a). The bench has the coupling coefficient as shown in Fig. 7, and the power transmission starts at −120 mm and stops at 110 mm. The velocity of the secondary coil is 10 km/h. The experiments compare about without control, phase shift control [31], and the proposed method ($I_{2\text{ref}}$ = 14 A, $E_{2\text{ref}}$ = 26 V) under constraint conditions, respectively.

Fig. 10 shows the experimental results for the transient parts. The response speed of the proposed method is sufficiently fast even when the coupling coefficient changes, and it seems there is no effect on the transient response control. The proposed method has the fastest settling time. Also, the currents decreased as time progressed because the coupling coefficient increased. In all experimental results, the amplitude of i_2 eventually settled on about 14 A.

Table II shows the results of the maximum current in the transient section and the receiving energy. The receiving energy was calculated from AC using oscilloscope values. Regarding the maximum current of i_2, the phase shift control did not overshoot during the transient and was the best result, followed by the proposed method, which caused a slight overshoot. Note that the overshoot was effect by L_m variation depending on the coil position. For the receiving energy up to 3 ms, the proposed method increased by about 44 % compared to the phase shift control. In addition, the proposed method has an effectiveness of energy efficiency, which is a ratio of energies up to 3 ms. Compared to without control, the proposed method also had almost the same receiving energy. The whole receiving energy after 3 ms was 20.85 J.

From the results, the conventional method has a long settling time while suppressing the current overshoot. On the other hand, the proposed method is effective in both current overshoot suppression and the amount of receiving energy.

These results show the small-scale case of about 300 W. If assuming the 30 kW condition, the receiving energy up to 3 ms may be close to about 90 J.

V. Conclusion

The paper proposes the method to suppress current overshoot at the start of power transmission focusing on rectification timing for dynamic wireless power transfer systems. The proposed method focuses on the superposition of the response from V_1 and V_2 to I_2. It is simple, requiring only switching at a steady-state current under a voltage constraint. Also, the robustness of the proposed method constraints has been evaluated based on model analysis and experiments. The proposed method has been demonstrated by experiments at static and dynamic conditions. The proposed method can suppress current overshoot effectively compared to without control even if constraints violate. In the best condition, the overshoot has been reduced to about 5 % while the switching time is only 68 μs. Furthermore, the experiment using the DWPT bench has confirmed the effectiveness of the receiving energy. In the transient section, the proposed method has increased the energy by about 44 % compared to the conventional control.

VI. Acknowledgement

This work was partly supported by JST-Mirai Program Grant Number JPMJMI21E2, JSPS KAKENHI Grant Num-

ber JP18H03768, and the New Energy and Industrial Technology Development Organization (NEDO) Project Number JPNP21005, Japan.

REFERENCES

[1] S. Li and C. C. Mi, "Wireless power transfer for electric vehicle applications," *IEEE J. Emerg. Sel. Top. Power Electron.*, vol. 3, no. 1, pp. 4–17, 2015.

[2] H. Zhang, Y. Shao, N. Kang, H. Qin, C. Ma, and M. Liu, "A Vertically Modularized Reconfigurable Wireless Power Transfer System: Architecture, Modeling, and Design," *IEEE Trans. Power Electron.*, vol. 38, no. 2, pp. 2730–2742, 2022.

[3] H. Matsumoto, T. Zaitsu, R. Noborikawa, Y. Shibako, and Y. Neba, "Control for Maximizing Efficiency of Three-Phase Wireless Power Transfer Systems At Misalignments," *IEEJ J. Ind. Appl.*, vol. 9, no. 4, pp. 401–407, 2019.

[4] A. Hakemi, D. Jovanovic, D. M. Vilathgamuwa, G. Walker, and J. Pauls, "Generic Uncertainty Parameter Analysis and Optimization of Series-Series Wireless Power Transfer System for Robust Controller Design," *IEEE Trans. Ind. Electron.*, vol. 69, no. 4, pp. 4107–4118, 2022.

[5] J. Zhou, B. Zhang, W. Xiao, D. Qiu, and Y. Chen, "Nonlinear Parity-Time-Symmetric Model for Constant Efficiency Wireless Power Transfer: Application to a Drone-in-Flight Wireless Charging Platform," *IEEE Trans. Ind. Electron.*, vol. 66, no. 5, pp. 4097–4107, 2019.

[6] V. D. Doan, T. Koseki, H. Kishi, H. Fujimoto, T. Yasuda, and T. Fujita, "Simultaneous optimization of speed profile and allocation of wireless power transfer system for autonomous driving electric vehicles," *IEEJ J. Ind. Appl.*, vol. 7, no. 2, pp. 189–201, 2018.

[7] A. C. Bagchi, A. Kamineni, R. A. Zane, and R. Carlson, "Review and Comparative Analysis of Topologies and Control Methods in Dynamic Wireless Charging of Electric Vehicles," *IEEE J. Emerg. Sel. Top. Power Electron.*, vol. 9, no. 4, pp. 4947–4962, 2021.

[8] G. Li and H. Ma, "A Hybrid IPT System With High-Misalignment Tolerance and Inherent CC-CV Output Characteristics for EVs Charging Applications," *IEEE Journal of Emerging and Selected Topics in Power Electronics*, vol. 10, no. 3, pp. 3152–3160, 2022.

[9] C. Cai, M. Saeedifard, J. Wang, P. Zhang, J. Zhao, and Y. Hong, "A Cost-Effective Segmented Dynamic Wireless Charging System With Stable Efficiency and Output Power," *IEEE Transactions on Power Electronics*, vol. 37, no. 7, pp. 8682–8700, 2022.

[10] K. Shi, C. Tang, Z. Wang, X. Li, Y. Zhou, and Y. Fei, "A Magnetic Integrated Method Suppressing Power Fluctuation for EV Dynamic Wireless Charging System," *IEEE Transactions on Power Electronics*, vol. 37, no. 6, pp. 7493–7503, 2022.

[11] S. Y. Jeong, J. H. Park, G. P. Hong, and C. T. Rim, "Autotuning Control System by Variation of Self-Inductance for Dynamic Wireless EV Charging with Small Air Gap," *IEEE Trans. Power Electron.*, vol. 34, no. 6, pp. 5165–5174, 2019.

[12] V. Z. Barsari, D. J. Thrimawithana, and G. A. Covic, "An Inductive Coupler Array for In-Motion Wireless Charging of Electric Vehicles," *IEEE Trans. Power Electron.*, vol. 36, no. 9, pp. 9854–9863, 2021.

[13] G. Guidi and J. A. Suul, "Transient Control of Dynamic Inductive EV Charging and Impact on Energy Efficiency when Passing a Roadside Coil Section," in *2018 IEEE PELS Work. Emerg. Technol. Wirel. Power Transf.*, 2018.

[14] X. Li, Y. Zhang, S. Chen, X. Zhang, and Y. Tang, "Coil Relative Position Transient Issue in Wireless Power Transfer Systems," *IEEE Trans. Ind. Electron.*, vol. 69, no. 3, pp. 2621–2630, 2022.

[15] F. Chen, H. Garnier, Q. Deng, M. K. Kazimierczuk, and X. Zhuan, "Control-Oriented Modeling of Wireless Power Transfer Systems with Phase-Shift Control," *IEEE Trans. Power Electron.*, vol. 35, no. 2, pp. 2119–2134, 2020.

[16] R. Tavakoli and Z. Pantic, "Analysis, Design, and Demonstration of a 25-kW Dynamic Wireless Charging System for Roadway Electric Vehicles," *IEEE J. Emerg. Sel. Top. Power Electron.*, vol. 6, no. 3, pp. 1379–1393, 2018.

[17] H. Feng and S. M. Lukic, "Reduced-Order Modeling and Design of Single-Stage LCL Compensated IPT System for Low Voltage Vehicle Charging Applications," *IEEE Trans. Veh. Technol.*, vol. 69, no. 4, pp. 3728–3739, 2020.

[18] S. Liu, R. Mai, L. Zhou, Y. Li, J. Hu, Z. He, Z. Yan, and S. Wang, "Dynamic Improvement of Inductive Power Transfer Systems with Maximum Energy Efficiency Tracking Using Model Predictive Control: Analysis and Experimental Verification," *IEEE Trans. Power Electron.*, vol. 35, no. 12, pp. 12 752–12 764, 2020.

[19] W. Shi, J. Dong, T. B. Soeiro, J. Deng, C. Riekerk, and P. Bauer, "Continuous Reduced-Order Dynamic Model Based on Energy Balancing for Inductive Power Transfer Systems," *IEEE Trans. Power Electron.*, vol. 37, no. 8, pp. 9959–9971, 2022.

[20] D. Kobayashi, T. Imura, and Y. Hori, "Real-time coupling coefficient estimation and maximum efficiency control on dynamic wireless power transfer for electric vehicles," in *2015 IEEE PELS Work. Emerg. Technol. Wirel. Power (2015 WoW)*. IEEE, 2015, pp. 1–6.

[21] J. Liu, Z. Liu, and H. Su, "Passivity-Based PI Control for Receiver Side of Dynamic Wireless Charging System in Electric Vehicles," *IEEE Trans. Ind. Electron.*, vol. 69, no. 1, pp. 783–794, 2022.

[22] K. Tokita, H. Fujimoto, and Y. Hori, "Feedforward Transient Control Under Varying Coupling Condition for In-motion Wireless Power Transfer Using Envelope Model," in *2020 IEEE Wirel. Power Transf. Conf.* IEEE, nov 2020, pp. 166–169.

[23] S. Lee and S.-H. Lee, "dq Synchronous Reference Frame Model of A Series–Series Tuned Inductive Power Transfer System," *IEEE Trans. Ind. Electron.*, vol. 67, no. 12, pp. 10 325–10 334, dec 2020.

[24] W. Shi, J. Deng, Z. Wang, and X. Cheng, "The Start-up Dynamic Analysis and One Cycle Control-PD Control Combined Strategy for Primary-Side Controlled Wireless Power Transfer System," *IEEE Access*, vol. 6, pp. 14 439–14 450, 2018.

[25] F. Farajizadeh, D. M. Vilathgamuwa, D. Jovanovic, P. Jayathurathnage, G. Ledwich, and U. Madawala, "Expandable N-Legged Converter to Drive Closely Spaced Multitransmitter Wireless Power Transfer Systems for Dynamic Charging," *IEEE Trans. Power Electron.*, vol. 35, no. 4, pp. 3794–3806, 2020.

[26] J. Jiang, K. Song, Z. Li, C. Zhu, and Q. Zhang, "System Modeling and Switching Control Strategy of Wireless Power Transfer System," *IEEE J. Emerg. Sel. Top. Power Electron.*, vol. 6, no. 3, pp. 1295–1305, 2018.

[27] K. Hata, T. Imura, H. Fujimoto, and Y. Hori, "Soft-Start Control Method for In-motion Charging of Electric Vehicles Based on Transient Analysis of Wireless Power Transfer System," in *2018 IEEE Energy Convers. Congr. Expo.* IEEE, sep 2018, pp. 2009–2015.

[28] T. Feng, Y. Sun, X. Dai, Y. Su, Z. Wang, C. Tang, and Z. Zuo, "Research on fast soft-starting methods for electric vehicle dynamic wireless charging system," in *2020 IEEE PELS Work. Emerg. Technol. Wirel. Power Transf.*, 2020, pp. 341–345.

[29] K. K. Prasad and V. Agarwal, "A Novel Frequency Modulation Technique to Minimize the Start-Up Transients in Dynamic Wireless Charging Systems for Electric Vehicles," in *2022 Wirel. Power Week, WPW 2022 - Proc.*, vol. 2022-Janua. IEEE, 2022, pp. 834–838.

[30] J. Noeren and N. Parspour, "Model predictive control for contactless energy transfer systems," in *2020 IEEE PELS Work. Emerg. Technol. Wirel. Power Transf.*, 2020, pp. 6–9.

[31] W. Zhong, H. Li, S. Y. Hui, and M. D. Xu, "Current Overshoot Suppression of Wireless Power Transfer Systems with on-off Keying Modulation," *IEEE Trans. Power Electron.*, vol. 36, no. 3, pp. 2676–2684, 2021.

[32] T. Hamada and H. Fujimoto, "Start-Up Current Control with Fast Settling by Time-Adjustment of Active Rectification for Wireless Power Transfer Systems," in *2022 Wirel. Power Week, WPW 2022 - Proc.* IEEE, 2022, pp. 240–243.

[33] T. Fujita, T. Yasuda, and H. Akagi, "A Dynamic Wireless Power Transfer System Applicable to a Stationary System," *IEEE Transactions on Industry Applications*, vol. 53, no. 4, pp. 3748–3757, 2017.

Takumi Hamada (Graduate Student Member, IEEE) received the B.E. degree in engineering from the College of Engineering Sciences, University of Tsukuba, Ibaraki, Japan, in 2021. He is currently working toward the M.S. degree in electrical engineering with the Department of Advanced Energy, Graduate School of Frontier Sciences, University of Tokyo, Tokyo, Japan.

His research interest includes dynamic wireless power transfer for EVs.

Toshiyuki Fujita (Member, IEEE) received the B.S. degree in electrical engineering, the M.S. degree in physical electronics, and the Ph.D degree in electrical and electronic engineering from the Tokyo Institute of Technology, Tokyo, Japan, in 2008, 2010, and 2017, respectively. From 2010 to 2014, he was with Panasonic Corporation, Osaka, Japan. Since 2014, he has been with Technova Inc., Tokyo, Japan. Since 2019, he has been a Project Assistant Manager with the University of Tokyo, Tokyo, Japan. His research interests include WPT systems for electric vehicles, ac/dc converters, and its control methods. Dr. Fujita is a Member of IEE of Japan, the Society of Automotive Engineers of Japan, and the Japan Society of Applied Physics.

Hiroshi Fujimoto (Senior Member, IEEE) received the Ph.D. degree in electrical engineering from the Department of Electrical Engineering, University of Tokyo, Tokyo, Japan, in 2001.

In 2001, he was a Research Associate with the Department of Electrical Engineering, Nagaoka University of Technology, Niigata, Japan. From 2002 to 2003, he was a Visiting Scholar with the School of Mechanical Engineering, Purdue University, West Lafayette, IN, USA. In 2004, he was a Lecturer with the Department of Electrical and Computer Engineering, Yokohama National University, Yokohama, Japan, where he became an Associate Professor in 2005. He is currently a Professor with the University of Tokyo. His research interests include control engineering, motion control, nano-scale servo systems, electric vehicle control, and motor drive.

Dr. Fujimoto was a recipient of the best paper awards from the IEEE TRANSACTIONS ON INDUSTRIAL ELECTRONICS in 2001 and 2013, Isao Takahashi Power Electronics Award in 2010, and the Best Author Prize of SICE in 2010. He is a Senior Member of IEE of Japan. He is also a member of the Society of Instrument and Control Engineers, the Robotics Society of Japan, and the Society of Automotive Engineers of Japan.